



## Article

# Towards an Affordable Means of Surgical Depth of Anesthesia Monitoring: An EMG-ECG-EEG Case Study

Ejay Nsugbe <sup>1,\*</sup>, Stephanie Connelly <sup>2</sup> and Ian Mutanga <sup>2</sup><sup>1</sup> Nsugbe Research Labs, Swindon SN1 3LG, UK<sup>2</sup> Hereford County Hospital, Wye Valley NHS Trust, Hereford HR1 2BN, UK; stephconnelly12@gmail.com (S.C.); ianrodney008@gmail.com (I.M.)

\* Correspondence: ennsugbe@yahoo.com

**Abstract:** The anesthetic dosing procedure is a key element of safe surgical practice, where it is paramount to ensure sufficient dosing of the anesthetic agent to the patient in order to reach the desired depth of sedation for the necessary procedure. One means of monitoring the depth of anesthesia (DoA) involves the use of the bispectral index (BIS), which decodes electroencephalography (EEG) signals acquired from the frontal cortex in a continuous fashion. The shortcomings of this include the complexity of the decoding of EEG signals, insensitivity to certain anesthetic agents, and the costly nature of the technology, which limits its adoption in resource-constrained settings. In this paper, we investigate an alternative source of physiological measurement modalities that can track DoA sufficiently while being much more affordable. Thus, we investigate this notion with the use of the University of Queensland database, which comprises EEG-EMG-ECG physiological data from patients going through a variety of surgical procedures. As part of this, select patient datasets were utilized in addition to a variety of signal decomposition and machine learning models—which totaled around 200 simulations—in order to investigate the most optimal combination of algorithms to track DoA using different physiological measurement modalities. The results showed that under certain algorithmic combinations and modeling processes, the ECG measurement (a ubiquitous monitor in anesthetic practice) can rival and occasionally surpass the accuracy of the EEG for DoA monitoring. In addition to this, we also propose a 2-phase modeling process that involves an algorithmic selection stage followed by a model deployment stage. Subsequent work in this area is advised to involve the acquisition of more physiological data from a broader mix of patients in order to further validate the consistency of the findings made in this study.

**Keywords:** anesthesia; EEG; ECG; EMG; LSDL; wavelet; signal processing; AI

**Citation:** Nsugbe, E.; Connelly, S.; Mutanga, I. Towards an Affordable Means of Surgical Depth of Anesthesia Monitoring: An EMG-ECG-EEG Case Study. *BioMedInformatics* **2023**, *3*, 769–790. <https://doi.org/10.3390/biomedinformatics3030049>

Academic Editor: Hans Binder

Received: 19 June 2023

Revised: 19 July 2023

Accepted: 30 August 2023

Published: 4 September 2023



**Copyright:** © 2023 by the authors. Licensee MDPI, Basel, Switzerland. This article is an open access article distributed under the terms and conditions of the Creative Commons Attribution (CC BY) license (<https://creativecommons.org/licenses/by/4.0/>).

## 1. Introduction and Background

One of the key components of surgical processes is the dosing of anesthesia, which is managed by anesthetists and allows for the surgery itself to take place in a relatively painless fashion [1–4]. There are four recognized components of anesthesia: hypnosis, analgesia, amnesia, and muscle relaxation. An applied state of general anesthesia chiefly acts on the central nervous system, with the optimal dosing of the anesthetic agents being of key importance [4]. The measurement of the depth of anesthesia (DoA) has been an area for continued study amongst anesthesia researchers, where common metrics used for the measurement include the bispectral index (BIS), entropy measurement, auditory evoked potentials (AEP), and the surgical stress index. Other avenues for quantifying the degree of pain include the analgesia nociception index (ANI) and the surgical pleth index (SPI) [2]. In the absence of specific DoA monitors, anesthesia dosing is based on the physiological response of the patient, and due to physiological differences, there is substantial variation of the sedation index amongst patients, making it difficult to foster a single index for the measurement of the DoA and sedation level [4].

Nevertheless, as part of safer surgical practices, continuous work has been conducted in optimal monitoring and DoA tracking to prevent complications from over or under-dosing of anesthesia [5–8]. The most widely used monitor is the BIS, whose full model architecture is protected due to intellectual property and works with a combination of electroencephalography (EEG) alongside what is believed to be a spectrum of high-order statistics from the acquired EEG time series [5–8]. Indices spanning 0–100 (from isoelectric/low brain activity to awake) are presented in real-time, and its introduction into the surgical theater in 1996, when it received FDA clearance, has helped to significantly reduce anesthetic dosing-related medical errors [5–8].

The BIS monitor uses fine-scale neural oscillations from the frontal cortex of the brain as input for computing the DoA metrics, and with a more reflective DoA measure, better recovery and wake-ups have now been noted after major surgery [9,10]. Nevertheless, the BIS monitor itself is only as accurate as its physiological measurement source, which in this case is EEG signals from the frontal cortex [11]. However, EEG has limitations, including: complexity and being difficult to decode; being non-reflective of cognitive state when drugs like ketamine and nitrous oxide are administered; sensitivity to interference; and being generally more expensive than other forms of physiological sensors [4,9,10]. This has prompted alternate exploration of physiological signals such as electrocardiograms (ECG) for DoA monitoring, which has been investigated by a number of authors, from whom it has been steadily observed that anesthetic information can be seen from rhythmic to nonrhythmic observations from an accompanying ECG signal [12–18].

The appeal of this form of physiological measurement as an inference for DoA is amplified by the fact that ECG signals and recording mechanisms are cheap to acquire and not as complex to process, which makes the adoption of this modality appealing to resource-constrained environments. However, previous studies have shown that the monitoring prowess and accuracy of ECG relative to EEG are slightly lower, which forms part of the investigation in this work [4]. For the first time in the published literature, bespoke advanced signal processing methods are adopted in the DoA prediction pipeline in an attempt to enhance the prediction accuracy of the candidate model as part of a potential low-cost anesthesia DoA monitoring platform. As part of this, we utilize physiological data from patients under various depths of anesthesia to perform a comparison study amongst modalities such as EEG, ECG, and an auxiliary physiological monitor, namely, electromyography (EMG). Data from several patients are utilized alongside various advanced signal processing methods using machine learning methods of different architectures [19,20].

The aforementioned advanced signal processing mechanism comprises a signal decomposition preprocessing mechanism and is followed by the extraction of a select list of features that form the core of a feature vector that is eventually used to train a machine learning model that serves as the prediction model [20]. Signal decomposition methods are a type of multiresolution approach typically utilized for the systematic separation of a candidate signal into subcomponents in order to find an optimal region within the signal, which minimizes noise and redundancies and boosts the modeling prowess of the signal. Common examples that have been applied within the area of DoA include the empirical mode decomposition and the wavelet decomposition, to name a few.

This work showcases, for the first time in the published literature, the application of the metaheuristically driven linear series decomposition learner (LSDL) and the deep wavelet scattering (DWS) method towards the decomposition of ECG and EMG physiological signals for anesthesia depth estimation [21,22]. Despite both of these being decomposition algorithms, they are underpinned by different decomposition configurations towards the systematic separation of the signal into component parts; hence, their respective performances are contrasted as part of the work done in this paper.

Once the features are extracted from a signal, a machine-learning model is typically utilized for the pattern recognition of the input data in association with an output label. In medicine, machine learning has played the role of data-driven prediction machines, which have been applied and deployed in various capacities. Machine learning models span

various architectures, from statistically driven discriminant analysis and logistic regression to decision tree and nearest neighbor models, all the way to models with more complex architectures such as support vector machines and deep learning models, to name a few [14]. A variety of these models have been researched and applied to serve as decision support in areas such as diabetes care, psychiatry, oncology, pregnancy care, and, of course, anesthesia DoA, where the introduction of these models has contributed towards a human-machine interaction platform that allows for enhanced clinical decision making and better patient care [23–26].

With respect to the work being presented in this paper, machine learning modeling represents the final stage of the signal processing pipeline where metrics and predictions are output and are meaningfully comprehensible to the end operator and clinician. In this work, seven different machine learning models were trained and utilized for the analysis in order to understand which combination of physiological sensing modality/signal decomposition method/machine learning yields optimal DoA estimation performance. Thus, a cumulative total of around 200 simulations were carried out as part of the work done in this study.

The contributions presented as part of this manuscript are as follows:

- Investigation of alternative physiological monitors that could contribute towards forming a low-cost avenue towards DoA monitoring by comparing the performance of ECG and EMG monitors with that of the traditionally used EEG;
- Premier use of signal decomposition methods such as the LSDL and DWS for the preprocessing and decomposition of ECG and EMG signals from anesthetized patients, with a view towards enhancing the DoA information that can be decoded and inferred from the signal;
- Comparison of the DoA estimation prowess across multiple classification models of varied model architecture complexities.

All the analytics yielded around 200 simulations across the pilot group of patients' data, covering the various physiological measurement modalities. Given the proposed contributions of the work, it is hypothesized that the groundwork would be laid for an affordable pipeline for DoA monitoring comprising a physiological monitor as well as the postprocessing algorithms and machine learning models. This would have a higher level of appeal to developing nations as well as resource-constrained environments.

## 2. Materials and Methods

### 2.1. Dataset and Information

The dataset utilized as part of this paper is from the University of Queensland Vital Signs Dataset, which has received ethical approval from both the Royal Adelaide Hospital and the University of Queensland and has the goal of acquiring physiological measurements from patients during various surgical procedures [27]. A number of supporting modules were used as part of the data acquisition process, as can be seen in the source publication, where data were acquired at what is believed to be around 100 Hz and stored in CSV format. The acquisitions were cropped to ensure that the data recordings reflected the commencement of the induction phase, while the end also reflected the removal of the sensor from the head after emergence [27].

It needs to be mentioned that all cases recorded as part of the database represent mostly minor surgeries with no traumatic events, while the effects of the prior medication before the surgery and anesthetic procedure were not taken into consideration in order to avoid a subjective view of the effect of the anesthetic agent on the patient [27].

Based on the research needs of the paper, three unique case studies were selected from the data on the basis of the patient having spent a long enough time under anesthesia and having data present for the BIS, EMG, ECG, and EEG. The BIS was selected as the ground truth label to support all subsequent modeling activities in consistency with the authors' prior work in this area. The classification case studies were then subsequently created, as seen in Table 1.

**Table 1.** Summary of classification case studies.

Case Study	Signal Windowing	Classification Exercise	Total Time Utilized (Minutes)
Case 1	9000 samples × 19 (for all modalities)	BIS Over 40 and Under 40	28.5
Case 2	6000 samples × 19 (for all modalities)	BIS Over 20 and Under 20	19
Case 3	9000 samples × 19 (for all modalities)	BIS Over 40 and Under 40	28.5

The windowing of the signal was chosen to be between 6000 and 9000 samples to account for 60–90 s worth of anesthetic dosing time, which is considered to be a robust window and segment time for all the modalities being considered. The classification exercise was formulated based on the dynamic range of the BIS monitor in order to establish a suitable DoA region where enough samples could be collected, all of which ensured minutes’ worth of samples were used as part of all modeling exercises. A hierarchical flow diagram of the various analytics done as part of the work presented in this paper for a sample patient can be seen in Figure 1.

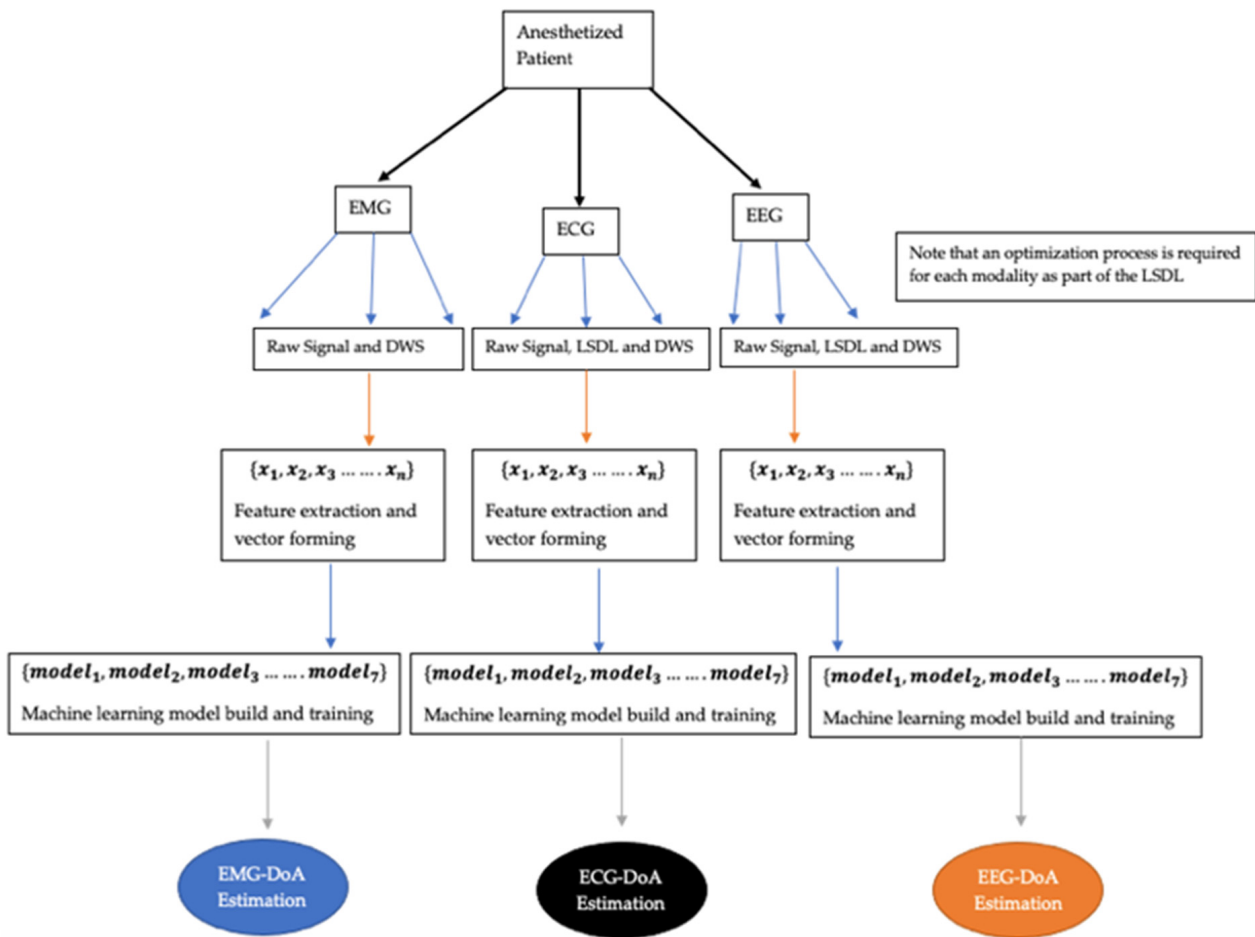


**Figure 1.** A hierarchical flow diagram of the various analytics done as part of the work presented in this paper for a sample patient.

Uncertainties: no patient demographic information; no details on the types of surgery done; a relatively small BIS variation range; only a small list of patients met the selection criteria.

### 2.2. Physiological Measurement Instrumentations

Although the work presented is not solely based upon theoretical simulations, the underpinning mathematical physics models behind the anatomical and physiological manifestations under certain given conditions are articulated and described as part of this subsection. In essence, these models quantify mathematical extracellular action potentials, which are acquired in a real-world scenario using physiological sensors.

#### 2.2.1. EMG

The concept of electrophysiological signals is themed around a transient flow of bio-electricity within a segment of muscle fibers. This flow is measured using a set of EMG electrodes, which are typically placed some distance from the source.

Using the principles of biophysics, this electrophysiological manifestation can be framed from the perspective of volume conduction and the 3-dimensional Ohm’s law formulation in a biological tissue [28–31]. Given the conductivity  $\sigma$ , the 3-dimensional acquisition point  $P_0(x_0, y_0, z_0)$ , with uniform conductivity  $\sigma_i$ , from a source current  $I_s$ , at point  $P(x, y, z)$ , can be formulated as Equation (1):

$$V_{p_0} = \frac{1}{4\pi\sigma_i} \frac{I_s}{r_i} \tag{1}$$

where  $V_{p_0}$  is a voltage potential, and  $r_i$  is the shortest distance between  $P_0$  and  $P$ . From Equation (1), an acquired voltage from a given point carries proportionality to the intensity of the source current, with the voltage potential being particularly inhibited by the distance and conductivity factors.

The dipole is frequently used as a physics-based approximation to represent a source generator, which is surrounded by a field of sorts [28–31]. For a fiber of length  $dx$  in the range of a given action potential, as the current flows into an extracellular region with the hypothetical focus of the magnitude being along the axis, this can be modeled as  $p^- \cdot dx$ , where  $p^-$  is the dipole current per unit length [28–31]. The source current permeates into free space in a dipole propagation characteristic, which thus leads to Equation (2), which can be said to hold for an extracellular potential:

$$d\varnothing_e = \frac{1}{4\pi\sigma_e} \cdot \frac{d\left(\frac{1}{r}\right)}{dx} \cdot p^-(x, t) dx \tag{2}$$

where  $\sigma_e$  is the conductivity of the extracellular mechanism and  $r$  is the source distance from the point of excitation to the instrumentation recording point  $P_0$ . For an element  $p^- \cdot dx$  along the coordinates  $(x, y, z)$  and  $P_0$  at  $(x_0, y_0, z_0)$ , the distance can then be formulated as Equation (3):

$$r = [(x - x_0)^2 + (y - y_0)^2 + (z - z_0)^2]^{\frac{1}{2}} \tag{3}$$

from which the total field can be estimated using the summations of the series of potentials from the resulting dipole current element, as can be seen in Equation (4):

$$\varnothing_e(x_0, y_0, z_0, t) = \int_{x=-\infty}^{x=\infty} \frac{p^-(x, t)}{4\pi\sigma_e [(x - x_0)^2 + y_0^2 + z_0^2]^{\frac{3}{2}}} dx \tag{4}$$

where  $t$  is time.

Note that in reality, the excitation source is likely to comprise a series of dipoles from a surface area, which represents an acquisition area.

#### 2.2.2. EEG

EEG signals refer to mostly passive measurements that acquire electric field activities from the brain, which are said to encode information on the neurological state of the patient [32,33]. The mathematical models used to quantitatively describe EEG manifes-

tations are based on the forward problem, with assumptions made for the model for the head and a conductivity overlay of the tissues within the skull [32,33]. As with the descriptions of the EMG, dipoles are useful approximations for the theoretical modeling of bio-electric manifestations within the brain. Using this basis and a series-based expansion approach, a 3-dipole approximation in a homogenous sphere has been utilized for the solution to a 4-layer spherical head model [32,33]. Thus, a multilayer head model  $L$  with concentric spheres with radii spanning  $0 < r_1 < r_2 \dots r_L$ , with anisotropic conductivities  $\sigma_1, \dots, \sigma_L$ . For a singular dipole at a point  $S$  within proximity of a sphere of a radius  $r_s < r_1$  with a moment  $q$ , an electric potential  $u$  measured at a point  $x$ , located at the farthest sphere  $\|x\| = r_L$  can thus be expressed as Equation (5):

$$\begin{aligned}
 u(r, q, x) &= \frac{|q|}{4\pi\sigma_L r_L^2} \\
 &= \sum_{n=1}^{\infty} \frac{2n+1}{n} \left(\frac{r_s}{r_L}\right)^{n-1} f_n [n\cos\alpha P_n(\cos\gamma) \\
 &\quad + \cos\beta\sin\alpha P_n^1(\cos\gamma)]
 \end{aligned}
 \tag{5}$$

where  $\alpha$  is the angle between  $S$  and the measurement acquisition point  $x$ , and  $\gamma$  is an angle between two planar vectors  $S$  and  $q$  on a specific side, and  $S$  and  $x$  on the other, while  $P_n$  and  $P_n^1$  are the Legendre polynomial coefficients in the series. The case of  $f_n$ , which corresponds to the  $n$ th element of the EEG measurement, can be calculated as seen in Equation (6):

$$f_n = \frac{n}{nm_{22} + (1+n)m_{21}}
 \tag{6}$$

where the coefficients  $m_{22}$  and  $m_{21}$  of the matrix  $m_{ij} \ 1 \leq i, j \leq 2$  can be obtained from Equation (7):

$$\begin{aligned}
 &\begin{bmatrix} m_{11} & m_{12} \\ m_{21} & m_{22} \end{bmatrix} \\
 &= \frac{1}{(2n+1)^{L-1}} \prod_{i=1}^{L-1} \begin{bmatrix} n + \frac{(n+1)\sigma_i}{\sigma_{i+1}} & (n+1)\left(\frac{\sigma_i}{\sigma_{i+1}} - 1\right)\left(\frac{r_L}{r_i}\right)^{2n+1} \\ n\left(\frac{\sigma_i}{\sigma_{i+1}} - 1\right) & (n+1) + \frac{n\sigma_i}{\sigma_{i+1}} \end{bmatrix}
 \end{aligned}
 \tag{7}$$

### 2.2.3. ECG

The ECG is a widely used tool for the recording of heart activity, but despite its widespread use, there continue to be apparent areas of uncertainty centered around it. The use of quantitative mathematical models has always provided an alternate insight into the mathematical and biophysical descriptions of a particular phenomenon [34]. The process of said quantitative modeling of a candidate set of ECGs is regarded as the forward modeling process, for which three assumptions and components are considered, namely: a model of the electrical activity of the heart; a model of the extracardiac regions of the torso; and some heart–torso conditions [34]. The complexity of the subsequent mathematical models hinges on the depth of the assumptions made as part of the forward modeling process. In this work, a 12-lead ECG model is described based on the work done by Boulakia et al. [34]. The components of this model are bidomain equations, phenomenological cell models, and generalized Laplacian equations to account for the torso [34].

#### - Heart Tissue

The electrical dynamics of the heart are accounted for using a bidomain model and work with the postulation that, on a cellular scale, cardiac tissue acts as an ohmic conducting medium that is separated by a cell membrane, both intracellular and extracellular, comprising cardiac and the space between them, respectively [35–37]. All of this occupies a whole volume  $\Omega_H$ , alongside intracellular and extracellular density  $j_i$  and  $j_e$ , conductivity tensors  $\sigma_i$  and  $\sigma_e$ , and electric potential  $u_i$  and  $u_e$ . The conservation of the electrical charge

thus becomes  $div(j_i + j_e) = 0$  in  $\Omega_H$ , where the homogenous representation of the electrical activity of the cell membrane is given as  $A_m \left( C_m \frac{\partial V_m}{\partial t} + I_{ion}(V_m, w) \right) + div(j_i) = A_m I_{app}$  in  $\Omega_H$ , with the Ohm's law representation  $j_i = -\sigma_i \nabla u_i$  and  $j_e = -\sigma_e \nabla u_e$ .  $V_m$  represents the transmembrane potential represented as  $V_m = u_i - u_e$ .

$A_m$  represents a constant of the rate of membrane area per unit volume, and  $C_m$  is the membrane, capacitance per unit area.  $I_{ion}(V_m, w)$  is the ionic current across the membrane and  $I_{app}$  is a given applied current stimulus, both of which are measured in terms of the membrane area unit [35–37]. The ionic current is a vectorized quantity  $w$  that fulfills a system of ODEs of the format  $\frac{\partial w}{\partial t} + g(V_m, w) = 0$ , in  $\Omega_H$ .  $g$  and  $I_{ion}$  are dependent upon the cell ionic current, where their levels of complexity are either phenomenological or physiological [35–37].

A scaled phenomenological 2-variable model is considered part of this model and expressed as Equations (8) and (9):

$$I_{ion}(V_m, w) = -\frac{w}{\tau_{in}} \frac{(V_m - V_{min})^2 (V_{max} - V_{in})}{V_{max} - V_{min}} + \frac{1}{\tau_{out}} \frac{V_{in} - V_{min}}{V_{max} - V_{min}} \tag{8}$$

$$g(V_m, w) = \begin{cases} \frac{w}{\tau_{open}} - \frac{1}{\tau_{open}(V_{max} - V_{min})^2} \text{ if } V_m < V_{gate} \\ \frac{w}{\tau_{close}} \text{ if } V_m > V_{gate} \end{cases} \tag{9}$$

where  $\tau_{in}$ ,  $\tau_{out}$ ,  $\tau_{open}$ ,  $\tau_{close}$ , and  $V_{gate}$  are fixed parameters, while  $V_{min}$  and  $V_{max}$  represent scaling constants.  $w$ , the gating variable, is stringent upon the  $V_{gate}$  voltage and associated time constants  $\tau_{open}$  and  $\tau_{close}$ . The timing constants  $\tau_{in}$  and  $\tau_{close}$  are linked to the length of both the depolarization and repolarization stages [35–37]. Thus, the system of equations that represents the electrical activity of the heart can be expressed as Equation (10):

$$\begin{cases} A_m \left( C_m \frac{\partial V_m}{\partial t} + I_{ion}(V_m, w) \right) \\ -div(-\sigma_i \nabla V_m) - div(-\sigma_i \nabla u_e) = A_m I_{app}, \text{ in } \Omega_H \\ -div((\sigma_i + \sigma_e) \nabla u_e) - div(\sigma_i \nabla V_m) = 0, \text{ in } \Omega_H \\ \frac{\partial V_m}{\partial t} + g(V_m, w) = 0, \text{ in } \Omega_H \end{cases} \tag{10}$$

As far as boundary conditions go, given  $V_m^0$  and  $w^0$  for the transmembrane potential and gate variable respectively, an initial condition of the form  $V_m(x, 0) = V_m^0(x)$ ,  $w(x, 0) = w^0(x) \forall x \in \Omega_H$  would be in place. With regards to the boundary conditions at the point  $\Sigma = \partial\Omega_H$ , with the assumption that the intracellular current does not propagate outside of the heart, we can then say  $j_i \cdot n = \sigma_i \nabla u_i \cdot n = 0$ , for  $\Sigma$ , where  $n$  is the outward unit to the normal of  $\Omega_H$  [35–37].

Figure 2 shows a summary of the various physiological organs, their basic operating principles, and their physiological sensing modalities, along with the associated pros and cons and a sample time series segment from a patient under anesthesia [38–40]. From the time series, the different dynamics in their respective physiological measurements can be noted. The EMG signal represents an enveloped variant of a raw EMG time series segment characterized by discrete fluctuations. The ECG signal is characterized by overlapping traditional QRS waveforms, which show the cyclical patterns of the human heart alongside its biophysical tendencies to be regarded as a biological pump mechanism. The EEG time series signal shows a continued series of neural oscillations that are highly superimposed, largely due to the multitude of oscillatory frequencies that brainwaves span, where there can also be seen to exist a high degree of noise as a result of the overall complexity of the organ itself [38–40].

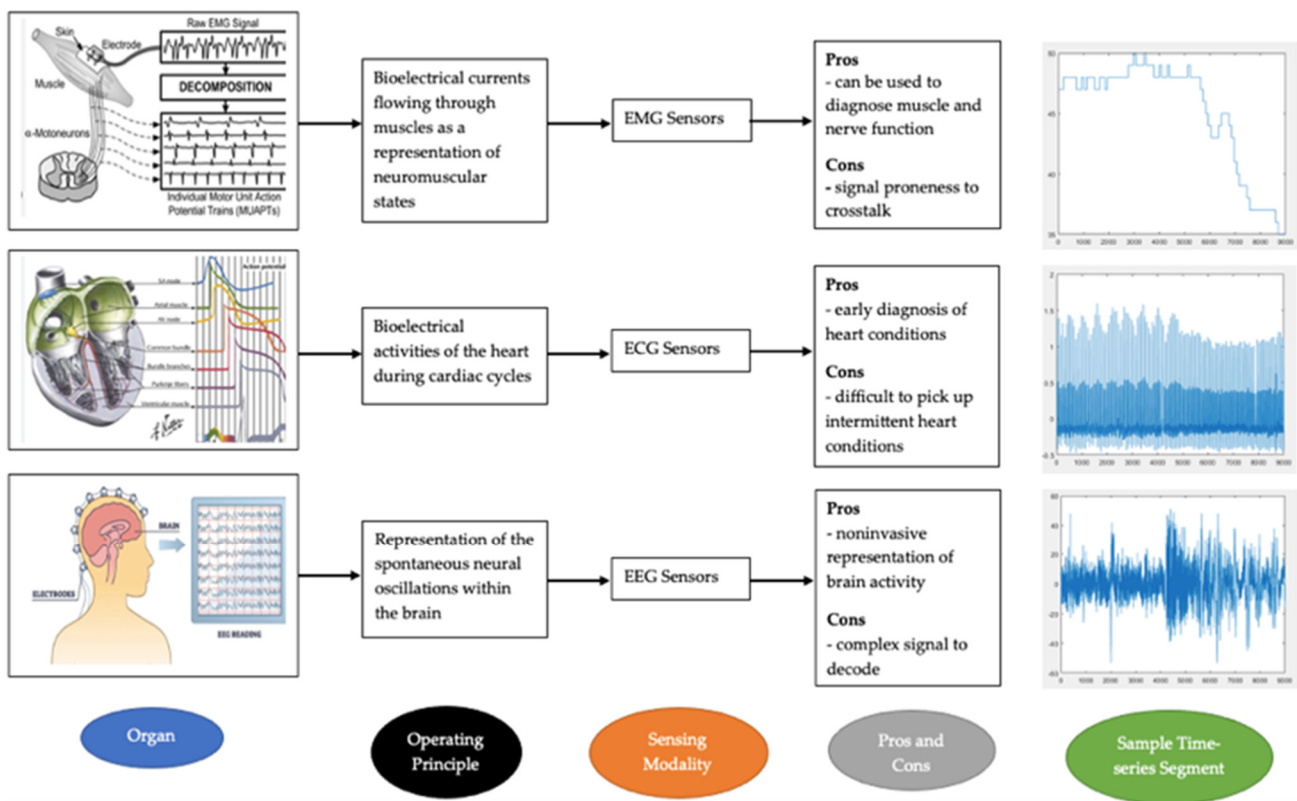


**Figure 2.** Summary of the various physiological organs, their basic operating principles, and physiological sensing modality, alongside the associated pros and cons, and a sample time series segment from a patient under anesthesia [38–40].

The set of plots in Figure 3 show the waveforms for a candidate patient across the various BIS values, i.e., over and under, where the left column represents the various time series projections of the physiological signals and the right column showcases the time-frequency view of the signals via the short time Fourier transform (STFT) spectrogram [41]. From the top down, the first two signals represent the ECG measurements, which are characterized by a stream of overlapping sharp peaks in the time domain and are reflected in the spectrogram as a cluster of information in the lower-mid frequency regions. From a visual perspective of the ECG-based spectrogram, it can be assumed that the rich content of the signal is in and around the earlier portion of the frequency spectrum. The subsequent set of plots is for the EMG signals, where it can be noted that an enveloped variant of the EMG signals was stored as opposed to the raw time series, which in general represents a fairly high amplitude signal and whose STFT representation yields a very low frequency transformation of the signal. Despite this, the resulting frequency representation appears to reflect a manifestation that is typically adjourned in the signal processing literature, in that the bulk of the frequency content related to neuromuscular EMG signals tends to be very low-frequency-based.

The final set of plots belongs to the EEG signals, which can be seen to represent a rather noisy and stochastic time series plot. This is largely due to the fact that the brain is physiologically viewed as a more complex organ than both the heart and muscle tissue but also operates on a varied set of frequency states that range from delta, theta, alpha, beta, and gamma [42]. Thus, from an abstraction standpoint, a sample resulting EEG waveform could comprise components and superpositions of the various brain states. Due to this, it can be seen that the frequency manifestations of the signal mostly symbolize a broadband phenomenon, which, although suggesting that a span of frequency components is a part of the signal itself, also shows that the bulk of the signal’s frequency information is intensely within the early portion of the frequency spectra.

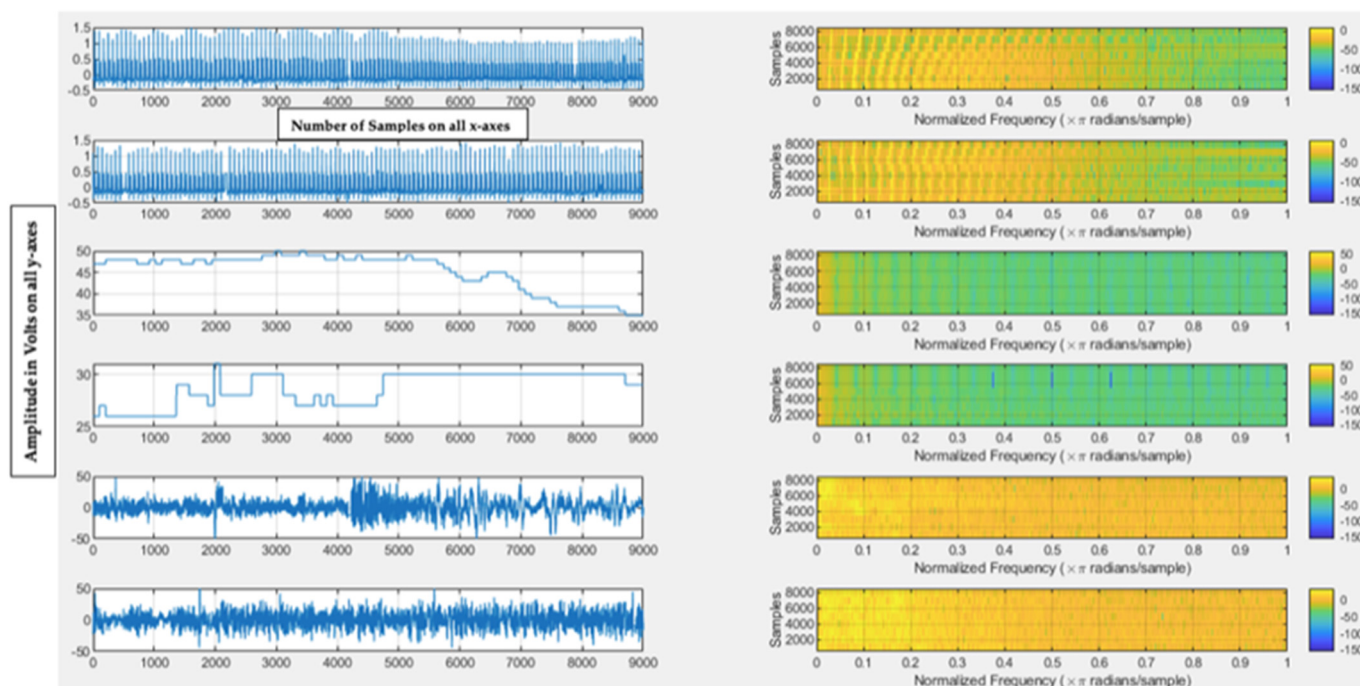


**Figure 3.** Waveforms for a candidate patient across the various BIS values, i.e., over and under. Left side: the various time series projections of the physiological signals. Right side: the time-frequency view of the signals via the short-time Fourier transform (STFT) spectrogram. Top two rows: ECG signals. Middle two rows: EMG signals. Bottom two rows: EEG signals.

### 2.3. Signal Decomposition

#### 2.3.1. LSDL

As mentioned, the use of signal decomposition methods aims towards the systematic separation of a candidate signal into component parts as a way of boosting the overall quality of a signal, where the LSDL is one that is embedded upon metaheuristic reasoning from the area of artificial intelligence [43–45]. The process involves using a set of defined heuristics as well as a linear basis function as part of the decomposition process to split the signal into subsections, which are assessed using an embedded cost function [43–45]. The application of the LSDL was initially for source separation of signals from powder mixtures, from which it was seen that the performance of the LSDL superseded that of the classical wavelet transform from both prediction accuracy and computational time perspectives when decomposing highly nonlinear and stochastic signals [43–45]. Subsequent application of the LSDL has seen its use as a key preprocessing tool in an array of areas within clinical medicine where physiological time series are acquired, including rehabilitation, preterm pregnancy, and psychiatric medicine; and very recently, it has also been applied to infrared spectroscopy waveforms in the early prediction of reproductive cancers in both males and females [25,46–48].

The LSDL comprises an in-built performance index that is able to assess the information quality of each of the decomposed regions obtained from the heuristic-based segmentation of the signal. The normalized Euclidean distance metric was utilized as the embedded performance index of choice for the LSDL, for which, given two candidate signals from two distinct classes, the normalized Euclidean distance provides a dimensionless metric that represents the distance and, therein, class separability between the two sample sets [49]. A flow diagram of this can be seen in Figure 4, which showcases the various stages involved in the LSDL's optimal region selection phase. For a full list of the designated heuristics as part of the LSDL, as well as the threshold parameters, Nsugbe et al. [46] and Nsugbe and Sanusi [47] contain more details.  $n$  was selected as 3 for the work done in this paper.

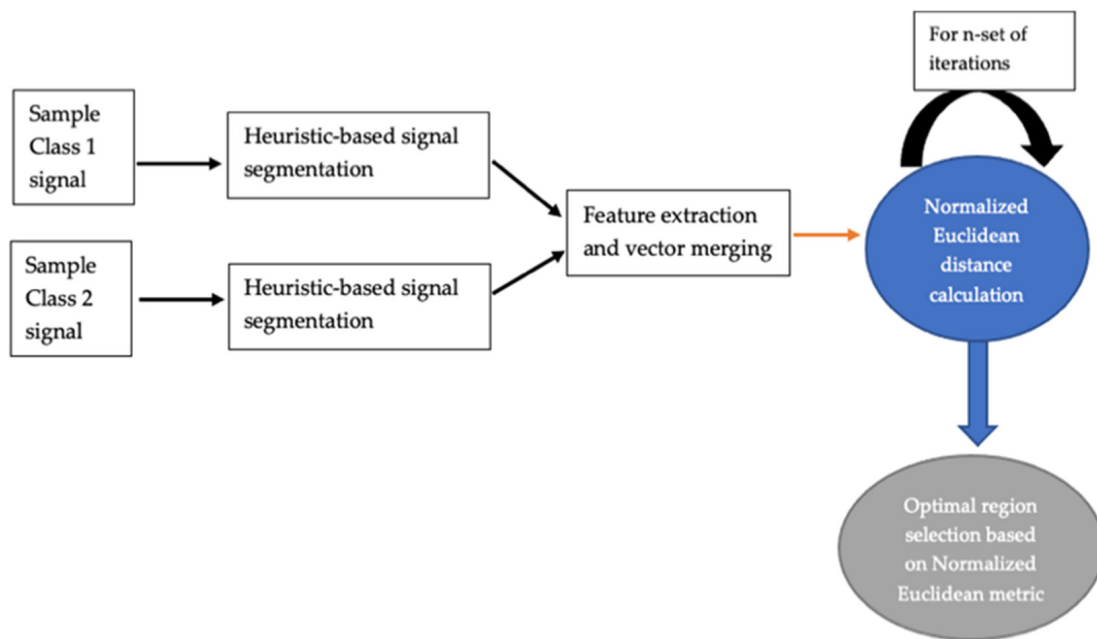


**Figure 4.** The various stages involved in the LSDL’s optimal region selection phase.

2.3.2. Optimal Threshold Search Results

As patient-specific DoA estimation models were designed as part of this paper, a specific DoA model was designed per patient, for which there were two physiological measurement modalities as the EMG could not be decomposed with the LSDL due to the format in which the data was recorded and captured. For each set of result tables, 12 optimization simulations were carried out in order to yield six sets of threshold “goodness” metrics. This was done for the two different measurement modalities to yield 24 optimization simulations per patient, for a total of 72 across all three patients.

The LSDL optimization results for the various patients and their associated modalities can be seen in Tables 2–7, from which it can be seen that the optimal decomposition for all patients and all modalities appears to be within the 3rd iteration of the upper threshold region, which indicates that the optimal information of the signal is within the high amplitude and low-frequency region.

Case Study 1

**Table 2.** LSDL optimization results for ECG.

Threshold Region	1st Iteration	2nd Iteration	3rd Iteration
Upper Threshold Region	2.0026	2.0093	2.2619
Lower Threshold Region	2.0000	2.0002	2.0046

**Table 3.** LSDL optimization results for EEG.

Threshold Region	1st Iteration	2nd Iteration	3rd Iteration
Upper Threshold Region	2.0092	2.0390	2.1723
Lower Threshold Region	2.0212	2.0013	2.0066

Case Study 2

**Table 4.** LSDL optimization results for ECG.

Threshold Region	1st Iteration	2nd Iteration	3rd Iteration
Upper Threshold Region	2.5750	2.7190	2.8217
Lower Threshold Region	2.0111	2.0020	2.0080

**Table 5.** LSDL optimization results for EEG.

Threshold Region	1st Iteration	2nd Iteration	3rd Iteration
Upper Threshold Region	2.2981	2.4454	2.4794
Lower Threshold Region	2.0371	2.0654	2.1704

Case Study 3

**Table 6.** LSDL optimization results for ECG.

Threshold Region	1st Iteration	2nd Iteration	3rd Iteration
Upper Threshold Region	2.7864	2.7901	2.7996
Lower Threshold Region	2.7040	2.6994	2.7071

**Table 7.** LSDL optimization results for EEG.

Threshold Region	1st Iteration	2nd Iteration	3rd Iteration
Upper Threshold Region	2.5842	2.5956	2.6032
Lower Threshold Region	2.2822	2.1494	2.0004

The threshold parameters used to obtain the optimal threshold regions shown in Tables 2–7 were used to perform any subsequent decomposition performed, when the LSDL algorithm was utilized.

- DWS

The DWS presents an unsupervised signal decomposition and multiresolution approach that uniquely combines characteristics from both the classical wavelet decomposition and the deep learning architectures [50–52]. Its features are continuous as well as robust to translations, with preset wavelets and filters as opposed to the traditional iterative learning from data [50–52]. One of the strengths of the DWS is its ability to work with a small set of data. Figure 5 shows a flow diagram summarizing the various sub-stages and key properties of the DWS, which include convolutions via wavelets, modulus nonlinearity, and averaging via a scaling function [50–52].

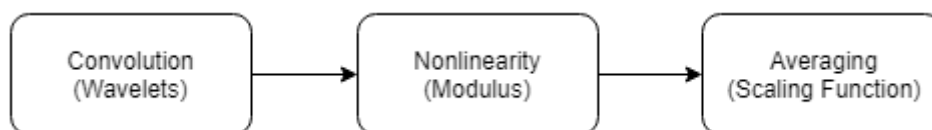


**Figure 5.** Stages of the deep wavelet scattering (DWS) method [52].

For a signal  $f(t)$  being analyzed with  $\emptyset$  being a low pass filter and a wavelet function of  $\Psi$  for filtering and decomposition, the wavelet family indices possess an octave frequency

resolution  $Q_k$  and are denoted as  $\wedge_k$ , alongside multiscale high pass filter banks  $\{\Psi_{jk}\}_{jk \in \wedge_k}$ , which are assembled via dilation of the wavelet  $\Psi$ , for which  $\emptyset_J(t)$  represents a low pass filter that is able to provide a localized translation invariance of the signal  $f(t)$  at a defined  $T$  [50–52].

The DWS is typically implemented using a convolutional neural network (CNN) which, based on its architecture, first performs convolutions through classical wavelets, which are followed by a nonlinear modulus, and finally by the averaging process [50–52]. The convolutional process is indicated as  $S_0f(t) = f * \emptyset_J(t)$ , for which  $S_0$  represents the zero-order scattering coefficients, which produce locally translation-invariant features for the signal  $f$ , which initially conveys a loss in high-frequency information but is duly recouped with the wavelet modulus  $|W_1|$ , as expressed in Equation (11) [50–52]:

$$|W_1|f = \{S_0f(t), |f * \Psi_{j1}(t)|\}_{j1 \in \wedge_1} \tag{11}$$

In a hierarchical tree-like fashion, the first set of scattering coefficients emanates from an averaging process of the wavelet modulus coefficient  $\emptyset_J(t)$ , as seen in Equation (12):

$$S_1f(t) = \{|f * \Psi_{j1}(t)| * \emptyset_J(t)\}_{j1 \in \wedge_1} \tag{12}$$

Information is lost due to the effect of the averaging process, but this can be subsequently recovered via the use of a wavelet modulus as part of the information recovery process, as expressed in Equation (13):

$$|W_2||f * \Psi_{j1}| = \{S_1f(t), ||f * \Psi_{j1}| * \Psi_{j2}(t)|\}_{j2 \in \wedge_2} \tag{13}$$

This is succeeded by the set of second-order coefficients, which can be defined as  $S_2f(t) = \{|f * \Psi_{j1}| * \Psi_{j2}| * \emptyset_J(t)\}_{j1 \in \wedge_1}$   $i = 1, 2$ , and continuously iterated via the described process to yield Equation (14):

$$U_mf(t) = \{|f * \Psi_{j1}| * \dots * |\Psi_{jm}|\}_{j1 \in \wedge_1}, i = 1, 2, \dots m. \tag{14}$$

for which  $U_m$  is an  $m$ th-order modulus. The  $m$ th order scattering coefficients for  $U_mf(t)$  with  $\emptyset_J$  can be obtained via Equation (15):

$$S_mf(t) = \{|f * \Psi_{j1}| * \dots * |\Psi_{jm}| * \emptyset_J(t)\}_{j1 \in \wedge_1}, i = 1, 2, \dots m \tag{15}$$

The described approach is applied in an iterative fashion to obtain a final scatter matrix  $Sf(t) = \{S_mf(t)\}_{0 \leq m \leq l}$ , which represents a concatenation of all the prior scatter coefficients, as a means of characterizing the input signal, for which  $l$  indicates the maximum decomposition level [50–52].

A tree-like visualization of the scattering decomposition network can be seen in Figure 6.

Since the DWS is comprised of the dual characteristics of the classical wavelets and the CNN, it is robust to translation invariance as well as stable to local deformations. The main difference between the DWS and the CNN is that the final output of the DWS is a combination of the output from a multitude of preceding layers and not primarily from an output layer [50–53].

The physics of the energy dissipation within the DWS networks suggest that the energy attenuates with an increasing number of layers, which is why only the first two layers within the network are utilized for modeling purposes and have thus been adopted in this work [50–53]. The remainder of the configuration parameters used as part of the DWS include the Gabor wavelet as the mother wavelet and basis function, an invariance scale of 1 s, and 8 wavelets per octave in the primary filter bank, followed by 1 wavelet per octave in the second filter bank [54].

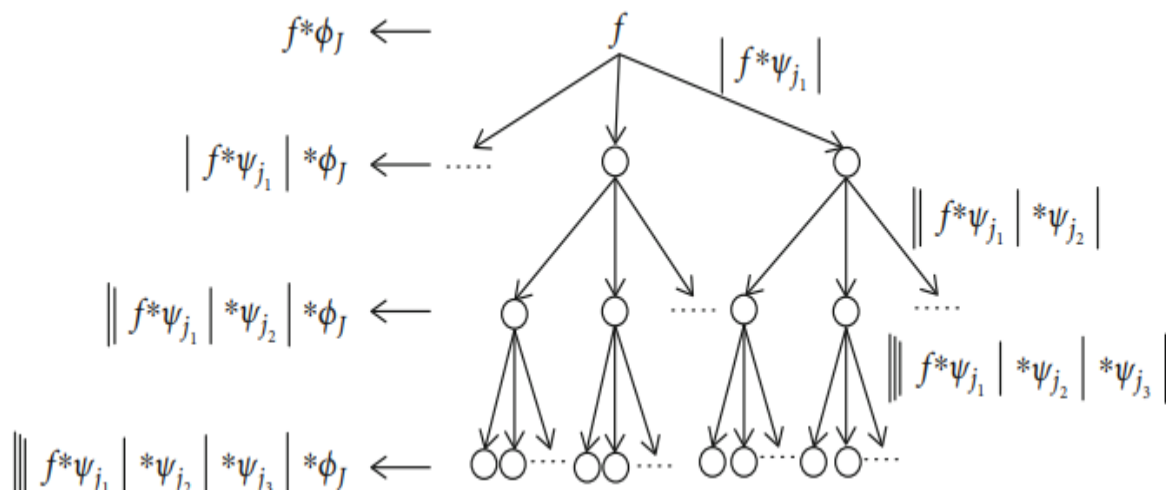


**Figure 6.** A tree-like visualization of the scattering decomposition network.

### 2.3.3. Feature Extraction

Several features were extracted from the EMG, ECG, and EEG signals, comprising a unique ensemble and concatenation of linear and nonlinear features, which can contribute towards the effective modeling of the various physiological signals [31]. The list of features is as follows: mean absolute value (MAV), waveform length (WL), zero-crossing (ZC), slope sign change (SSC), root mean square (RMS), fourth-order autoregression (AR), sample entropy (SampEN), cepstrum (Ceps), maximum fractal length (MFL), median frequency (MedFrq), peak frequency (PeakFrq), number of peaks (NP), simple squared integral (SSI), and variance (VAR) [31]. A threshold of  $1 \mu\text{v}$  was used for all features that required a threshold, and the values of 2 and 0.2 were used for the  $m$  and  $r$  variables for the sample entropy feature [31].

### 2.3.4. Machine Learning Models

Decision Tree (DT): refers to a class of gray-box models that hinge upon Boolean logic as a systemic means towards class separation for the various sample sets in a hierarchical flow fashion [55]. Due to the configuration of the model, its decision-making process carries a degree of interpretability [55].

Logistic Regression (LR): is a form of statistically underpinned parametric model that outputs class scores in the range of 0–1 and then interpolates based on a threshold score to find out which class the sample set belongs to [56]. A sigmoidal function is used for interpolation purposes and provides an extra layer of robustness when dealing with outliers [56].

K-Nearest Neighbor (KNN): is a nonparametric classification model that utilizes a combination of majority voting and nearest neighbor criteria for the assignment of samples into various classes. In this work, the value for  $k$  was selected to be 1 in the interest of computational efficiency, while the Euclidean distance was adopted as the distance metric of choice [57].

Support Vector Machine (SVM): is based around the assumption that higher dimensions are better suited for the class separation of data classes that are within proximity of each other in a lower-dimensional space [58]. Class boundaries are placed in an iterative fashion in a higher-dimensional subspace, and their boundary coordinates are retained during the downscaling of the data projection, a feat regarded as a “kernel trick” [58]. The model is viewed as computationally intensive due to the requirement for coordinate transformation and iterative fitting of class boundaries [58]. In this work, a number of variants of the decision boundaries were used to separate the various classes, namely, linear SVM-LSVM, quadratic SVM-QSVM, cubic SVM-CSVM, and fine Gaussian SVM-FGSVM.

All models were built and validations were done using the MATLAB Classification Learner Application, which tunes models for the most appropriate hyperparameters given the pattern recognition task. All models were validated using the K-fold cross validation method, with K chosen as 10.

### 3. Results and Discussion

#### 3.1. Case Study 1

Classification Problem: BIS over 40 and under 40

Table 8 shows the results for the raw signal modeling for Case Study 1.

**Table 8.** Results for modeling with the raw signal for BIS over 40 and under 40.

Machine Learning Model	Raw EMG Accuracy (%)	Raw ECG Accuracy (%)	Raw EEG Accuracy (%)	Raw EMG-ECG-EEG Accuracy (%)
Decision Tree	44.7	52.6	65.8	31.6
Logistic Regression	42.1	47.4	44.7	34.2
K-Nearest Neighbor	47.4	52.6	47.4	47.4
Linear Support Vector Machine	34.2	36.8	76.3	57.9
Quadratic Support Vector Machine	52.6	52.6	50.0	57.9
Cubic Support Vector Machine	44.7	34.2	65.8	60.5
Fine Gaussian Support Vector Machine	42.1	50.0	57.9	50.0

For the modeling with the raw signal, it can be seen for the EMG that the results are fairly mediocre, with the best prediction accuracy being the QSVM model at 52.6%, while the same trend appears to happen for the ECG, with the DT and QSVM providing the best prediction performance. The EEG produced the best accuracy in this scenario, with an accuracy metric of 76.3% for the LSVM, which was also seen to supersede the fusion of the features from the three various modalities. Table 9 shows the results for the LSDL.

**Table 9.** Results for modeling with the LSDL for BIS over 40 and under 40.

Machine Learning Model	LSDL ECG Accuracy (%)	LSDL EEG Accuracy (%)
Decision Tree	55.3	60.5
Logistic Regression	89.5	86.8
K-Nearest Neighbor	47.4	76.3
Linear Support Vector Machine	44.7	73.7
Quadratic Support Vector Machine	44.7	78.9
Cubic Support Vector Machine	47.4	76.3
Fine Gaussian Support Vector Machine	26.3	65.8

For the LSDL, the ECG provided a best accuracy of 89.5%, while the EEG provided 86.8%, both for the logistic regression model, which further showcases the compatibility between the LSDL and the logistic regression, as has been noted in a previous study [47]. However, it needs to be noted that although the ECG provided the best overall accuracy, the mean of all classifiers across the board for the EEG was seen to be greater than the ECG. Nevertheless, the combination of the LSDL for preprocessing and the logistic regression model showed that the ECG produces an exceedingly better performance when compared with that of the EEG. The results for the DWS can be seen in Table 10.

**Table 10.** Results for modeling with the DWS for BIS over 40 and under 40.

Machine Learning Model	DWS EMG Accuracy (%)	DWS ECG Accuracy (%)	DWS EEG Accuracy (%)
Decision Tree	67.8	74.9	66.9
Logistic Regression	61.2	76.2	70.5
K-Nearest Neighbor	66.3	88.6	98.0
Linear Support Vector Machine	58.9	74.2	69.1
Quadratic Support Vector Machine	53.3	88.5	87.4
Cubic Support Vector Machine	51.8	90.8	94.7
Fine Gaussian Support Vector Machine	59.5	84.2	85.8

The DWS provided better prediction accuracy for the EMG signal, as a best performance metric of 67.8% was recorded. Strong metrics were seen to be provided for both the ECG and EEG modalities at 90.8% and 98.0%, respectively, albeit for different models, i.e., CSVM and KNN. This provides strong evidence for the decomposition power of the DWS when encountering physiological signals of this kind.

Table 11 shows a summary of the best prediction accuracies across the various pre-processing approaches and classification models. It can be seen that for this patient and under the observed conditions, the DWS was the optimal preprocessing mechanism, where the ECG was within 10% of the EEG, which further shows its appeal and potential as a low-cost anesthesia monitor, and also that the optimal classification model varied based on the modality being used for the patient.

**Table 11.** Summary of the best prediction accuracies across the various preprocessing approaches and classification models for Case Study 1.

Best Modality	Best Prediction Accuracy (%)
EMG	DWS DT: 67.8
ECG	DWS CSVM: 90.8
EEG	DWS KNN: 98.0

### 3.2. Case Study 2

Classification Problem: BIS over 20 and under 20

The results for the raw signal can be seen in Table 12, from which it can be noted that the EMG prediction accuracy is a high value of 84.2% for the DT and is believed to be largely due to the simplified classification problem relative to the prior patient's case study. Both the ECG and the EEG produced accuracies of 81.6% for the QSVM and DT, respectively, while the case of the modality feature fusion produced an accuracy of 84.2% for the DT model.

**Table 12.** Results for modeling with the raw signal for BIS over 20 and under 20.

Machine Learning Model	Raw EMG Accuracy (%)	Raw ECG Accuracy (%)	Raw EEG Accuracy (%)	Raw EMG-ECG-EEG Accuracy (%)
Decision Tree	84.2	71.1	81.6	84.2
Logistic Regression	50.0	71.1	73.7	63.2
K-Nearest Neighbor	52.6	47.4	47.4	47.4
Linear Support Vector Machine	50.0	76.3	73.7	78.9
Quadratic Support Vector Machine	50.0	81.6	78.9	78.9

**Table 12.** *Cont.*

Machine Learning Model	Raw EMG Accuracy (%)	Raw ECG Accuracy (%)	Raw EEG Accuracy (%)	Raw EMG-ECG-EEG Accuracy (%)
Cubic Support Vector Machine	50.0	78.9	81.6	78.9
Fine Gaussian Support Vector Machine	50.0	73.7	71.1	47.4

The results for the LSDL (Table 13) showed comparable metrics between the ECG and EEG, with the ECG delivering a slightly higher accuracy at 81.6% when compared with the EEG at 78.9%. The optimal classification model for both the ECG and EEG was the LR model.

**Table 13.** Results for modeling with the LSDL for BIS over 20 and under 20.

Machine Learning Model	LSDL ECG Accuracy (%)	LSDL EEG Accuracy (%)
Decision Tree	44.7	52.6
Logistic Regression	81.6	78.9
K-Nearest Neighbor	65.8	39.5
Linear Support Vector Machine	47.4	52.6
Quadratic Support Vector Machine	63.2	55.3
Cubic Support Vector Machine	65.8	65.8
Fine Gaussian Support Vector Machine	50.0	44.7

The results for the DWS can be seen in Table 14, showing a strong set of prediction metrics across all three modalities and once again indicating the compatibility of the DWS with these kinds of physiological datasets. The kernel-based SVM was the best-performing classification model, with prediction accuracies of 89.8%, 99.7%, and 98.5% for the EMG, ECG, and EEG modalities, respectively.

**Table 14.** Results for modeling with the DWS for BIS over 20 and under 20.

Machine Learning Model	DWS EMG Accuracy (%)	DWS ECG Accuracy (%)	DWS EEG Accuracy (%)
Decision Tree	85.7	96.5	90.6
Logistic Regression	73.7	98.8	93.0
K-Nearest Neighbor	87.4	98.8	98.0
Linear Support Vector Machine	89.8	95.9	93.6
Quadratic Support Vector Machine	88.6	99.4	97.7
Cubic Support Vector Machine	88.6	99.7	98.5
Fine Gaussian Support Vector Machine	86.8	95.9	84.8

Table 15 shows a summary of the best prediction accuracies across the various pre-processing approaches and classification models. It can be seen that the DWS was the best-performing preprocessing algorithm, which produced a 90%+ classification accuracy performance across all three measurement modalities, alongside the kernel-based SVM model. Once again, it can be noted that the ECG performance is within range of the EEG, thus showing its potential for being utilized to greater effect in this area, while the EMG also showed a high prediction performance for the DWS at this level of a deep sedation state.

**Table 15.** Summary of the best prediction accuracies across the various preprocessing approaches and classification models for Case Study 2.

Best Modality	Best Prediction Accuracy (%)
Best EMG	DWS LSVM: 89.8
Best ECG	DWS CSVM: 99.7
Best EEG	DWS CSVM: 98.5

### 3.3. Case Study 3

Classification Problem: BIS over 40 and under 40

The results for this case study show a generally low value for the EMG prediction accuracy, with the best performance being 55.3% for the case of the LSVM, as seen in Table 16. The ECG and the EEG both provided a prediction accuracy of 71.1% for the DT and CSVM, respectively, while the fusion of all modalities provided an accuracy of 76.3%.

**Table 16.** Results for modeling with the raw signal for BIS over 40 and under 40.

Machine Learning Model	Raw EMG Accuracy (%)	Raw ECG Accuracy (%)	Raw EEG Accuracy (%)	Raw EMG-ECG-EEG Accuracy (%)
Decision Tree	42.1	71.1	60.5	52.6
Logistic Regression	42.1	52.6	60.5	55.3
K-Nearest Neighbor	42.1	60.5	63.2	76.3
Linear Support Vector Machine	55.3	42.1	57.9	50.0
Quadratic Support Vector Machine	47.4	47.4	68.4	71.1
Cubic Support Vector Machine	47.4	50.0	71.1	76.3
Fine Gaussian Support Vector Machine	52.6	52.6	65.8	63.2

Table 17 shows that the LSDL provided a strong set of classification metrics for both the ECG and EEG for this case study, with the best prediction accuracy being in the region of 94.7% for the ECG, while the EEG produced a perfect 100% prediction accuracy across a select number of classifiers. Due to the number of uncertainties about the dataset itself, it remains unclear if the high metrics attained in this case were due to the patient demographic, the kind of surgery, or anesthetic constituents.

**Table 17.** Results for modeling with the LSDL for BIS over 40 and under 40.

Machine Learning Model	LSDL ECG Accuracy (%)	LSDL EEG Accuracy (%)
Decision Tree	94.7	97.4
Logistic Regression	94.7	100
K-Nearest Neighbor	89.5	100
Linear Support Vector Machine	94.7	100
Quadratic Support Vector Machine	94.7	100
Cubic Support Vector Machine	92.1	100
Fine Gaussian Support Vector Machine	84.2	92.1

The DWS provided a best prediction accuracy of 64% for the EMG modality alongside the DT model (see Table 18), while the ECG and EEG provided accuracies of 89.1% and 98.5%, respectively, showcasing high prediction accuracies for both modalities alongside the LSDL.

**Table 18.** Results for modeling with the DWS for BIS over 40 and under 40.

Machine Learning Model	DWS EMG Accuracy (%)	DWS ECG Accuracy (%)	DWS EEG Accuracy (%)
Decision Tree	64.0	72.3	68.0
Logistic Regression	57.1	75.7	71.7
K-Nearest Neighbor	63.4	89.1	98.5
Linear Support Vector Machine	56.8	76.5	69.8
Quadratic Support Vector Machine	51.2	87.9	87.6
Cubic Support Vector Machine	50.4	50.2	95.1
Fine Gaussian Support Vector Machine	59.9	77.9	89.5

Table 19 shows the best performances across all three modalities for Case Study 3, where it can be seen that the LSDL alongside the LR models prevail as the optimal means of signal preprocessing and classification. In the case of the EMG, the best performance was seen to be a combination of the DWS and DT.

**Table 19.** Summary of the best prediction accuracies across the various preprocessing approaches and classification models for Case Study 3.

Best Modality	Best Prediction Accuracy (%)
Best EMG	DWS DT: 64.0
Best ECG	LSDL Logistic Regression: 94.7
Best EEG	LSDL Logistic Regression: 100

As mentioned, despite the classification problem for this case study being similar to Case Study 1, the optimal processing and classification models appear to be different, as do the accuracies. It remains unclear as to whether this is due to the anesthetic agents used or the kind of surgery conducted, as it is difficult to comment in this direction due to the uncertainties in the description of the dataset itself.

The results in the various case studies provide a degree of numerical and statistical evidence that the ECG signals—when preprocessed and modeled with an effective processing mechanism—can indeed provide a comparable accuracy to that of the traditionally favored EEG monitor. However, it needs to be said that this inference has been made from a relatively concise sample set, which contains uncertainties and sparse information around the nature of the anesthetic dosing, the surgery, and the patients themselves. Nevertheless, using a data-driven lens to interpret the results, the accuracy figures for the ECG and EEG are proven to be comparable. While the EMG occasionally provides strong figures, it is simply not sufficient to work as a primary DoA monitor given the requirements for things in this setting.

Further insights from the results obtained suggest that, given the confines of the investigations carried out, there does not appear to be a “one size fit all” in terms of the best decomposition method and best model to utilize for the processing of the physiological signals; thus, the proposition made involves a 2-phase, multi-stage process for an affordable DoA monitoring platform. This is envisaged to have a strong level of appeal to developing countries and under-resourced areas.

The modeling flow can be seen in Figure 7, for which, given a patient-specific anesthetic DoA monitor, the first stage involves physiological data acquisition using an affordable modality in the form of an ECG monitor, followed by the application of various signal decomposition methods as part of the selection process, feature extraction, and then an iterative sorting using the candidate machine learning models. Once this is complete, the candidate modeling methods can then be deployed to perform a real-time DoA estimation

using the candidate decomposition and machine learning models, as indicated in the second phase of the flow diagram.

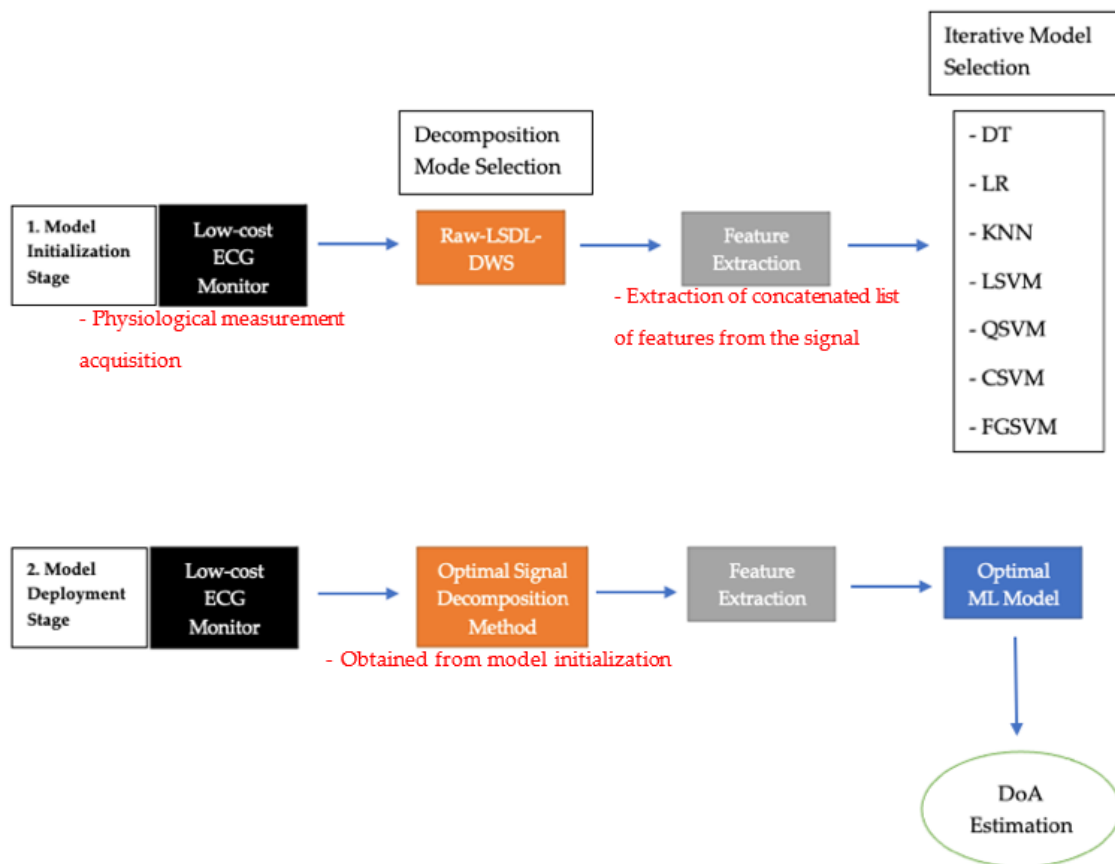


**Figure 7.** 2-phase process for an affordable DoA monitoring platform.

#### 4. Conclusions and Future Work

Sufficient depth of anesthesia is crucial for most surgical processes, where it is of paramount importance to be able to infer and estimate the degree of patient sedation. This is typically done with the use of physiological monitors, the EEG in particular, which monitors brainwaves from the frontal cortex as part of the BIS model. Despite its wide array of uses, EEG has limitations with regards to the ability to closely monitor sedation extent, for example, when certain drugs are used, in addition to being expensive and complex to decode. This has raised the appeal and potential of other modalities, such as EMG and ECG, as surrogate and affordable means towards DoA monitoring. Thus, this work utilized a physiological database from the University of Queensland [27], alongside an array of signal decomposition algorithms and machine learning models, to observe the extent to which other modalities compare to the likes of EEG when tasked with DoA monitoring. Around 200 simulations were run across three different patient datasets, alongside a comparative use of various signal decomposition methods and machine learning models.

Different classification challenges were constructed for each of the three patients, while the various associated physiological datasets were postprocessed. It was seen across the three patients that a singular “one size fits all” algorithmic signal processing pipeline does not exist for the postprocessing of the signals due to the varied physiological make-up of each patient, the anesthetic agent, and surgery procedures. Nevertheless, it was seen on multiple occasions that the ECG data was on par and within range of the EEG, providing further evidence as to how this modality could serve as a potential physiological monitor for DoA purposes in resource-constrained settings. The modeling and postprocessing pipeline for the dataset itself includes a selection stage due to the lack of a single optimal method across all patients.

Due to the dataset itself, there continue to be a number of areas of uncertainty; despite the results presented, there is no detailed information on the patient demographics, the surgical process itself, or the anesthetic agents used. All of this, plus a concise sample set, leads the authors to believe that more work would need to be done to validate the findings from the paper, with emphasis on the areas highlighted.

**Author Contributions:** All authors contributed equally to the article. All authors have read and agreed to the published version of the manuscript.

**Funding:** This research received no external funding.

**Informed Consent Statement:** Informed consent was obtained from all subjects involved in the study.

**Data Availability Statement:** The data is available from a cited repository within the manuscript.

**Acknowledgments:** The authors would like to thank Brian Kerr for proofreading the manuscript.

**Conflicts of Interest:** The authors declare no conflict of interest.

## References

- Alwardt, C.M.; Redford, D.; Larson, D.F. General Anesthesia in Cardiac Surgery: A Review of Drugs and Practices. *J. Extra Corpor. Technol.* **2005**, *37*, 227–235.
- Lan, J.-Y.; Abbod, M.F.; Yeh, R.-G.; Fan, S.-Z.; Shieh, J.-S. Review: Intelligent Modeling and Control in Anesthesia. *J. Med. Biol. Eng.* **2012**, *32*, 293–307.
- Gruenewald, M.; Ilies, C.; Herz, J.; Schoenherr, T.; Fudickar, A.; Höcker, J.; Bein, B. Influence of Nociceptive Stimulation on Analgesia Nociception Index (ANI) during Propofol-Remifentanyl Anaesthesia. *Br. J. Anaesth.* **2013**, *110*, 1024–1030. [[CrossRef](#)]
- Roy Chowdhury, M.; Madanu, R.; Abbod, M.F.; Fan, S.-Z.; Shieh, J.-S. Deep Learning via ECG and PPG Signals for Prediction of Depth of Anesthesia. *Biomed. Signal Process. Control* **2021**, *68*, 102663. [[CrossRef](#)]
- Kissin, I. Depth of Anesthesia and Bispectral Index Monitoring. *Anesth. Analg.* **2000**, *90*, 1114–1117. [[CrossRef](#)] [[PubMed](#)]
- Medical Advisory Secretariat. Bispectral Index Monitor: An Evidence-Based Analysis. *Ont. Health Technol. Assess. Ser.* **2004**, *4*, 1–70.
- Liu, Q.; Chen, Y.-F.; Fan, S.-Z.; Abbod, M.F.; Shieh, J.-S. Quasi-Periodicities Detection Using Phase-Rectified Signal Averaging in EEG Signals as a Depth of Anesthesia Monitor. *IEEE Trans. Neural Syst. Rehabil. Eng.* **2017**, *25*, 1773–1784. [[CrossRef](#)]
- Liu, Q.; Ma, L.; Chiu, R.-C.; Fan, S.-Z.; Abbod, M.F.; Shieh, J.-S. HRV-Derived Data Similarity and Distribution Index Based on Ensemble Neural Network for Measuring Depth of Anaesthesia. *PeerJ* **2017**, *5*, e4067. [[CrossRef](#)]
- Nsugbe, E.; Connelly, S. Multiscale Depth of Anaesthesia Prediction for Surgery Using Frontal Cortex Electroencephalography. *Healthc. Technol. Lett.* **2022**, *9*, 43–53. [[CrossRef](#)] [[PubMed](#)]
- Nsugbe, E.; Connelly, S. A Pilot on Intelligence Fusion for Anesthesia Depth Prediction during Surgery Using Frontal Cortex Neural Oscillations. *Biomed. Eng. Adv.* **2022**, *4*, 100051. [[CrossRef](#)]
- Ponde, V. Recent Trends in Paediatric Regional Anaesthesia. *Indian J. Anaesth.* **2019**, *63*, 746–753. [[CrossRef](#)]
- Tyers, M.R.; Russell, W.J.; Runciman, W.B. Electrocardiographic Monitoring in Anaesthesia. *Anaesth. Intensive Care* **1988**, *16*, 66–69. [[CrossRef](#)]
- Iohom, G. Basic Patient Monitoring during Anesthesia—UpToDate. Available online: <https://www.uptodate.com/contents/basic-patient-monitoring-during-anesthesia> (accessed on 10 June 2023).
- Zhou, Z.-H. *Machine Learning*; Springer Nature: Berlin, Germany, 2021; ISBN 9789811519673.
- Adarsh, S.L.; Venugopal Syam, K.; Philip, L.M.; Martin John, K.D.; Dileepkumar, K.M.; Krathiyani, K.; Ajithkumar, S.; Devanand, C.B. Electrocardiographic Evaluation of Balanced General Anaesthesia in Adult Domestic Cats (*Felis Catus*). *Indian J. Canine Pract.* **2022**, *14*, 22–24. [[CrossRef](#)]
- Jo, Y.-Y.; Jang, J.-H.; Kwon, J.; Lee, H.-C.; Jung, C.-W.; Byun, S.; Jeong, H.-G. Predicting Intraoperative Hypotension Using Deep Learning with Waveforms of Arterial Blood Pressure, Electroencephalogram, and Electrocardiogram: Retrospective Study. *PLoS ONE* **2022**, *17*, e0272055. [[CrossRef](#)] [[PubMed](#)]
- Obert, D.P.; Schweizer, C.; Zinn, S.; Kratzer, S.; Hight, D.; Sleigh, J.; Schneider, G.; García, P.S.; Kreuzer, M. The Influence of Age on EEG-Based Anaesthesia Indices. *J. Clin. Anesth.* **2021**, *73*, 110325. [[CrossRef](#)]
- Zhan, J.; Wu, Z.; Duan, Z.; Yang, G.; Du, Z.; Bao, X.; Li, H. Heart Rate Variability-Derived Features Based on Deep Neural Network for Distinguishing Different Anaesthesia States. *BMC Anesthesiol.* **2021**, *21*, 66. [[CrossRef](#)] [[PubMed](#)]
- Orfanidis, S.J. *Introduction to Signal Processing*; Prentice Hall Signal Processing Series; Prentice Hall: Englewood Cliffs, NJ, USA, 1996; ISBN 978-0-13-209172-5.
- Mallat, S.G. A Theory for Multiresolution Signal Decomposition: The Wavelet Representation. *IEEE Trans. Pattern Anal. Mach. Intell.* **1989**, *11*, 674–693. [[CrossRef](#)]
- Stallone, A.; Cicone, A.; Materassi, M. New Insights and Best Practices for the Successful Use of Empirical Mode Decomposition, Iterative Filtering and Derived Algorithms. *Sci. Rep.* **2020**, *10*, 15161. [[CrossRef](#)] [[PubMed](#)]

22. Soltani, S. On the Use of the Wavelet Decomposition for Time Series Prediction. *Neurocomputing* **2002**, *48*, 267–277. [[CrossRef](#)]
23. Kavakiotis, I.; Tsave, O.; Salifoglou, A.; Maglaveras, N.; Vlahavas, I.; Chouvarda, I. Machine Learning and Data Mining Methods in Diabetes Research. *Comput. Struct. Biotechnol. J.* **2017**, *15*, 104–116. [[CrossRef](#)]
24. Nsugbe, E. Enhanced Recognition of Adolescents with Schizophrenia and a Computational Contrast of Their Neuroanatomy with Healthy Patients Using Brainwave Signals. *Appl. AI Lett.* **2023**, *4*, e79. [[CrossRef](#)]
25. Nsugbe, E.; Ser, H.-L.; Ong, H.-F.; Ming, L.C.; Goh, K.-W.; Goh, B.-H.; Lee, W.-L. On an Affordable Approach towards the Diagnosis and Care for Prostate Cancer Patients Using Urine, FTIR and Prediction Machines. *Diagnostics* **2022**, *12*, 2099. [[CrossRef](#)] [[PubMed](#)]
26. Nsugbe, E. Towards the Use of Cybernetics for an Enhanced Cervical Cancer Care Strategy. *Intell. Med.* **2022**, *2*, 117–126. [[CrossRef](#)]
27. Liu, D.; Görges, M.; Jenkins, S.A. University of Queensland Vital Signs Dataset: Development of an Accessible Repository of Anesthesia Patient Monitoring Data for Research. *Anesth. Analg.* **2012**, *114*, 584–589. [[CrossRef](#)]
28. Rodriguez-Falces, J.; Navallas, J.; Malanda, A. Computational Intelligence in Electromyography Analysis—A Perspective on Current Applications and Future Challenges. In *Computational Intelligence in Electromyography Analysis—A Perspective on Current Applications and Future Challenges*; Naik, G.R., Ed.; IntechOpen: London, UK, 2012; ISBN 978-953-51-0805-4.
29. Cram, J.R.; Kasman, G.S.; Holtz, J. *Introduction to Surface Electromyography*; Aspen Publishers: Gaithersburg, MD, USA, 1998; ISBN 978-0-8342-0751-6.
30. Petersen, E.; Rostalski, P. A Comprehensive Mathematical Model of Motor Unit Pool Organization, Surface Electromyography, and Force Generation. *Front. Physiol.* **2019**, *10*, 176. [[CrossRef](#)]
31. Nsugbe, E.; Samuel, O.W.; Asogbon, M.G.; Li, G. Phantom Motion Intent Decoding for Transhumeral Prosthesis Control with Fused Neuromuscular and Brain Wave Signals. *IET Cyber-Syst. Robot.* **2021**, *3*, 77–88. [[CrossRef](#)]
32. Darbas, M.; Lohrengel, S. Review on Mathematical Modelling of Electroencephalography (EEG). *Jahresber. Dtsch. Math. Ver.* **2019**, *121*, 3–39. [[CrossRef](#)]
33. Doschoris, M.; Kariotou, F. Mathematical Foundation of Electroencephalography. In *Electroencephalography*; Sittiprapaporn, P., Ed.; IntechOpen: London, UK, 2017; ISBN 978-953-51-3638-5.
34. Boulakia, M.; Cazeau, S.; Fernández, M.A.; Gerbeau, J.-F.; Zemzemi, N. Mathematical Modeling of Electrocardiograms: A Numerical Study. *Ann. Biomed. Eng.* **2010**, *38*, 1071–1097. [[CrossRef](#)]
35. Pullan, A.J.; Cheng, L.K.; Buist, M.L. *Mathematically Modelling the Electrical Activity of the Heart: From Cell to Body Surface and Back Again*; World Scientific: Hackensack, NJ, USA, 2005; ISBN 978-981-256-373-6.
36. Sundnes, J.; Lines, G.; Cai, X.; Nielsen, B.F.; Mardal, K.-A.; Tveito, A. *Computing the Electrical Activity in the Heart*; Springer: Berlin/Heidelberg, Germany, 2006; ISBN 978-3-540-33432-3.
37. Tung, L. A Bi-Domain Model for Describing Ischemic Myocardial d-c Potentials. Ph.D. Thesis, Massachusetts Institute of Technology, Cambridge, MA, USA, 1978.
38. De Luca, C.J.; Adam, A.; Wotiz, R.; Gilmore, L.D.; Nawab, S.H. Decomposition of Surface EMG Signals. *J. Neurophysiol.* **2006**, *96*, 1646–1657. [[CrossRef](#)]
39. Sarazan, R.D. The QT Interval of the Electrocardiogram. In *Encyclopedia of Toxicology*, 3rd ed.; Wexler, P., Ed.; Academic Press: Oxford, UK, 2014; pp. 10–15, ISBN 978-0-12-386455-0.
40. Eeg and Brainwaves. Bright Brain—London’s Eeg, Neurofeedback and Brain Stimulation Centre. Available online: <https://www.brightbraincentre.co.uk/electroencephalogram-eeg-brainwaves/> (accessed on 29 August 2023).
41. Durak, L.; Arikan, O. Short-Time Fourier Transform: Two Fundamental Properties and an Optimal Implementation. *IEEE Trans. Signal Process.* **2003**, *51*, 1231–1242. [[CrossRef](#)]
42. Klimesch, W. The Frequency Architecture of Brain and Brain Body Oscillations: An Analysis. *Eur. J. Neurosci.* **2018**, *48*, 2431–2453. [[CrossRef](#)] [[PubMed](#)]
43. Nsugbe, E.; Starr, A.; Ruiz-Carcel, C. Monitoring the Particle Size Distribution of a Powder Mixing Process with Acoustic Emissions: A Review. *Eng. Technol. Ref.* **2016**, 1–12. [[CrossRef](#)]
44. Nsugbe, E. Particle Size Distribution Estimation of a Powder Agglomeration Process Using Acoustic Emissions. Ph.D. Thesis, Cranfield University, Cranfield, UK, 2017.
45. Nsugbe, E.; Starr, A.; Jennions, I.; Ruiz-Carcel, C. Estimation of Online Particle Size Distribution of a Particle Mixture in Free Fall with Acoustic Emission. *Part. Sci. Technol.* **2019**, *37*, 953–963. [[CrossRef](#)]
46. Nsugbe, E.; Williams Samuel, O.; Asogbon, M.G.; Li, G. Contrast of Multi-Resolution Analysis Approach to Transhumeral Phantom Motion Decoding. *CAAI Trans. Intell. Technol.* **2021**, *6*, 360–375. [[CrossRef](#)]
47. Nsugbe, E.; Sanusi, I. Towards an Affordable Magnetomyography Instrumentation and Low Model Complexity Approach for Labour Imminency Prediction Using a Novel Multiresolution Analysis. *Appl. AI Lett.* **2021**, *2*, e34. [[CrossRef](#)]
48. Nsugbe, E. On the Use of Spectroscopy, Prediction Machines and Cybernetics for an Affordable and Proactive Care Approach for Endometrial Cancer. *Biomed. Eng. Adv.* **2022**, *4*, 100057. [[CrossRef](#)]
49. Gower, J.C. Properties of Euclidean and Non-Euclidean Distance Matrices. *Linear Algebra Its Appl.* **1985**, *67*, 81–97. [[CrossRef](#)]
50. Wavelet Scattering. Available online: <https://uk.mathworks.com/help/wavelet/ug/wavelet-scattering.html> (accessed on 29 August 2023).
51. Mallat, S. Group Invariant Scattering. *Commun. Pure Appl. Math.* **2012**, *65*, 1331–1398. [[CrossRef](#)]

52. Bruna, J.; Mallat, S. Invariant Scattering Convolution Networks. *IEEE Trans. Pattern Anal. Mach. Intell.* **2013**, *35*, 1872–1886. [[CrossRef](#)]
53. Liu, Z.; Yao, G.; Zhang, Q.; Zhang, J.; Zeng, X. Wavelet Scattering Transform for ECG Beat Classification. *Comput. Math. Methods Med.* **2020**, *2020*, e3215681. [[CrossRef](#)] [[PubMed](#)]
54. Nsugbe, E. On the Application of Metaheuristics and Deep Wavelet Scattering Decompositions for the Prediction of Adolescent Psychosis Using EEG Brain Wave Signals. *Digit. Technol. Res. Appl.* **2022**, *1*, 9–24. [[CrossRef](#)]
55. Charbuty, B.; Abdulazeez, A. Classification Based on Decision Tree Algorithm for Machine Learning. *J. Appl. Sci. Technol. Trends* **2021**, *2*, 20–28. [[CrossRef](#)]
56. LaValley, M.P. Logistic Regression. *Circulation* **2008**, *117*, 2395–2399. [[CrossRef](#)] [[PubMed](#)]
57. Kramer, O. K-Nearest Neighbors. In *Dimensionality Reduction with Unsupervised Nearest Neighbors*; Intelligent Systems Reference Library; Springer: Berlin/Heidelberg, Germany, 2013; Volume 51, pp. 13–23, ISBN 978-3-642-38651-0.
58. Noble, W.S. What Is a Support Vector Machine? *Nat. Biotechnol.* **2006**, *24*, 1565–1567. [[CrossRef](#)]

**Disclaimer/Publisher’s Note:** The statements, opinions and data contained in all publications are solely those of the individual author(s) and contributor(s) and not of MDPI and/or the editor(s). MDPI and/or the editor(s) disclaim responsibility for any injury to people or property resulting from any ideas, methods, instructions or products referred to in the content.